PCCP

PAPER

View Article Online
View Journal | View Issue

Cite this: *Phys. Chem. Chem. Phys.*, 2018, **20**, 28452

Probing chirality recognition of protonated glutamic acid dimers by gas-phase vibrational spectroscopy and first-principles simulations†

Johanna Klyne, [a] Aude Bouchet, ‡[b] Shun-ichi Ishiuchi, [b] Masaaki Fujii, [b] Markus Schneider,[c] Carsten Baldauf[cd] and Otto Dopfer *[ae]

Received 17th September 2018,
Accepted 31st October 2018

DOI: 10.1039/c8cp05855e

rsc.li/pccp

The homochirality of the amino acid metabolism still puzzles biochemists. Vibrational spectroscopy of mass-selected gas-phase amino acids and their clusters can precisely reveal their conformation and might ultimately help to decode the interactions responsible for chirality recognition. Infrared photodissociation (IRPD) and conformer-selective IR–IR hole burning spectra of protonated glutamic acid dimers (LL-/LD-Glu_2H^+) recorded in the fingerprint and XH stretch ranges (1100–1900 and 2600–3600 cm^{-1}) provide direct insight into their stereospecific interactions. Glu_2H^+ dimers are generated by electrospray ionization and stored in a cryogenic quadrupole ion trap held at 10 K. The assignment of the IRPD spectra is supported by vibrational analysis using many-body dispersion-corrected hybrid density-functional theory. Sampling of the conformational space is accomplished by basin hopping and replica-exchange molecular dynamics simulations. The most stable LD-Glu_2H^+ dimer (LD1) is predicted to be more stable than the most stable LL-Glu_2H^+ dimer (LL1) by ΔE_0 = 4.0 kJ mol^{-1}, which relies on stronger secondary interactions in LD1 as demonstrated by the noncovalent interaction method. IR–IR hole burning spectroscopy reveals the coexistence of at least four LD-Glu_2H^+ and three LL-Glu_2H^+ conformers. Their IR-dip spectra are assigned to the most stable conformers at room and cryogenic temperature, revealing incomplete thermalization of the ions by kinetic trapping in the cold trap. We observe different population ratios of LL and LD conformers of Glu_2H^+, as revealed by specific ν_{NH_2} and ν_{CO} intensities (fingerprints of chirality recognition).

1. Introduction

In natural organisms, many chiral biomolecules, such as sugars or amino acids, almost exclusively possess a single handedness. The origin of this homochirality remains an open question.[1–6] In this context, two issues are discussed: how is an initial enantiomeric excess produced, and how is it amplified to result in homochirality? Several factors are discussed as driving forces for an initial imbalance in favour of a certain enantiomer, *i.e.* one of the two exact mirror images of a chiral molecule:

1. An imbalance may be induced by parity violation.[1–3] Parity describes the symmetry of a physical object with respect to point reflection of its spatial coordinates. For chiral systems it can be violated within the framework of electroweak interaction, leading to very small energy differences between enantiomers ($\approx 10^{-11}$ J mol^{-1}).[1,7] High-resolution gas-phase spectroscopic techniques have been applied to measure this intrinsic property of chiral molecules, so far without success.[7,8]

2. After an excess of L-amino acids on the Murchison meteorite has been observed,[9] extraterrestrial circularly-polarized radiation has been suggested as the chirality-determining factor on prebiotic earth.[4,5,10] Irradiation of a racemic mixture of amino acids with circularly-polarized ultraviolet light can indeed produce an enantiomeric excess in the laboratory,[11] even under conditions similar to an extraterrestrial environment.[12]

3. A small initial chiral excess may rest upon a statistical imbalance produced in a preceding chemical reaction.[6,13]

Since all three processes most likely result only in a minor imbalance, amplification based on chirality recognition

[a] *Institut für Optik und Atomare Physik, Technische Universität Berlin, Hardenbergstr. 36, 10623 Berlin, Germany. E-mail: dopfer@physik.tu-berlin.de*
[b] *Laboratory for Chemistry and Life Science, Institute of Innovation Research, Tokyo Institute of Technology, 4259, Nagatsuta-cho, Midori-ku, Yokohama, Japan. E-mail: mfujii@res.titech.ac.jp*
[c] *Fritz-Haber-Institut der MPG, Faradayweg 4-6, 14195 Berlin, Germany. E-mail: baldauf@fhi-berlin.mpg.de*
[d] *Wilhelm-Ostwald-Institut für Physikalische und Theoretische Chemie, Universität Leipzig, Linnéstr. 2, D-04103 Leipzig, Germany*
[e] *Tokyo Tech World Research Hub Initiative (WRHI), Institute of Innovation Research, Tokyo Institute of Technology, 4259, Nagatsuta-cho, Midori-ku, Yokohama, Japan*

† Electronic supplementary information (ESI) available. See DOI: 10.1039/c8cp05855e

‡ Present address: LASIR, CNRS UMR 8516, Université de Lille – Sciences et Technologies, 59655 Villeneuve d'Ascq, France.

is imperative. Different chemical and physical models, such as asymmetric amplification[14] or chiral autocatalysis,[15,16] are currently developed.[3] The chemical or physical amplification of an enantiomeric imbalance for a given molecular species can only happen by the formation of diastereomeric species (*e.g.*, a dimer of two chiral partners). Amplification is then based on the different physico-chemical properties of the diastereomeric species. To investigate if such preferential stereospecific pairing occurs in simple amino acid dimers, herein we study the structure-based recognition in homochiral (LL) and heterochiral (LD) dimers of glutamic acid (L-/D-Glu), one of the 20 natural amino acids.

While only L-amino acids are incorporated into naturally synthesized proteins, also detectable amounts of D-amino acids are found in mammalian tissues.[17,18] The anion of L-Glu, L-glutamate, is the principal excitatory neurotransmitter in the brain.[19–23] D-Glutamate can also bind to its receptors. However, glutamate transport is enantioselective,[24,25] illustrating the correlation between molecular handedness and biochemical function, *i.e.* chirality recognition.

Chirality recognition is defined as the preference to form one diastereomeric structure instead of the other because of different interactions between the two subunits of a contact pair. It is suggested to result from a subtle balance of inter- and intramolecular hydrogen bonds (H-bonds), and the decisive role of weak stereospecific interactions has been demonstrated.[26–28] The weak spectral signatures of these H-bonds may be hidden in the condensed phase. Therefore, sensitive gas-phase experiments are suitable for their detection in isolated tailor-made molecular clusters.[26,29,30] For example, mass spectrometry revealed the extraordinary self-organization of homochiral protonated serine (Ser) tetramers[4] and octamers,[31–33] that were hereupon presented as a possible origin for biomolecular homochirality.[34] A recent gas-phase vibrational spectroscopy study revealed an asymmetric, yet highly H-bonded structure for the Ser_8H^+ magic number cluster.[35] Structure and stability of serine dimers (Ser_2H^+) have been studied by means of mass spectrometry and quantum chemical calculations,[36–38] as well as infrared (IR) spectroscopy.[39,40] In an effort to unravel signatures of chirality recognition, the energy difference between homo- (LL) and heterochiral (LD) Ser_2H^+ was measured[36] and calculated[39] yielding ΔG of 0.2 ± 0.2 kJ mol^{-1} and 0.49 kJ mol^{-1}, respectively, in favour of the LL dimer. Furthermore, recent spectroscopic studies successfully demonstrated chirality recognition in neutral molecular clusters.[26–28,41] These studies have been expanded to ionic chiral molecules and clusters.[42–46]

Our present research rests on previous investigations by means of gas-phase spectroscopy and theory. Neutral Glu is rather flexible, resulting in 385 isomers predicted within $\Delta E \sim 75$ kJ mol^{-1}.[47–49] Five of these were detected by microwave spectroscopy in a cold molecular beam, all with an intramolecular NH···OC or N···HO H-bond between the α-carboxyl (α-COOH) and amino (NH_2) groups.[50] Protonation of the amino group ($NH_2 \rightarrow NH_3^+$) leads to conformational locking of $GluH^+$ by formation of strong cooperative HOCO···HNH^+···OCOH ionic H-bonds. As a consequence, only two almost isoenergetic isomers are observed in the gas phase.[47,51,52] Recently, our IRPD spectra of cryogenic $GluH^+$ revealed their relative abundance as approximately 2 : 1, showing the importance of cryogenic cooling, single-photon absorption conditions, and consideration of the XH stretch range (2600–3600 cm^{-1}) for the identification of molecular conformation.[51] IR spectra and quantum chemical analysis of alkali-metalated $GluM^+$ (M = Li-Cs) revealed cation size-dependent conformational locking by HOCO···M^+···OCOH bridges.[52–54] Herein, we apply cryogenic infrared photodissociation (IRPD) and IR–IR hole burning spectroscopy and first-principles simulations to homochiral (LL) and heterochiral (LD) glutamic acid dimers (LL-/LD-Glu_2H^+) to determine their structures, energies and eventually their chirality recognition.

2. Experimental and theoretical methods

We only give a brief overview of the experimental and computational techniques employed. Detailed descriptions are available in the ESI.†

2.1 IRPD spectroscopy

IRPD spectra of H_2-tagged LL-/LD-Glu_2H^+-H_2 dimers are recorded in the XH stretch (ν_{XH}; X = O, N; 2600–3600 cm^{-1}) and fingerprint ranges (1100–1900 cm^{-1}) employing a cryogenic quadrupole ion trap (QIT) tandem mass spectrometer.[55] LL-/LD-Glu_2H^+ ions are generated *via* electrospray ionization (ESI). To distinguish LL- and LD-Glu_2H^+ by means of mass spectrometry, L-Glu-2,3,3,4,4-d_5 (L-d_5-Glu) with five deuterium atoms at its alkyl chain is used. Moreover, ^{15}N-isotope labelling is employed to disentangle NH and OH stretches by IRPD spectroscopy. The ESI-generated LL-/LD-Glu_2H^+ ions are size-selected by a first quadrupole mass spectrometer and subsequently trapped in the QIT held at 10 K. He/H_2 (80 : 20) buffer gas pulses are injected into the QIT to form cold LL-/LD-Glu_2H^+-H_2. The trapped ions are irradiated by pulses of a tuneable IR optical parametric oscillator (bandwidth 1.7 cm^{-1}) pumped by a nanosecond injection-seeded Nd:YAG laser (10 Hz), to record IRPD spectra in the XH stretch and fingerprint ranges. Resonant vibrational excitation followed by fast internal vibrational energy redistribution induces dissociation of LL-/LD-Glu_2H^+-H_2 (loss of H_2). IRPD spectra are recorded *via* the fragment ion current in a time-of-flight mass spectrometer as a function of the IR laser frequency. We plot the fragmentation yield $R = I_f/(I_p + I_f)$, where I_p and I_f refer to the abundances of parent and fragment ions, respectively. All spectra are normalized for IR laser intensity fluctuations. The IR-OPO provides 0.7–10 mJ per pulse in the XH stretch range and 0.5–1.3 mJ per pulse in the fingerprint range.

2.2 IR–IR hole burning spectroscopy

IR–IR hole burning spectra of LL-/LD-Glu_2H^+-H_2 are recorded by setting the probe IR laser (bandwidth 3.5–5 cm^{-1}) at a conformer-specific transition in the IRPD spectrum, thereby generating a constant fragmentation signal. The pump IR laser is introduced into the QIT 3 ms before the probe laser, where

resonant excitation of any of the conformers present in the trap leads to fragmentation. All fragments induced by the pump laser are removed from the trap by a ''tickle'' RF pulse applied to the QIT before the probe laser is fired.[56,57] If the pump laser hits a transition of the conformer currently probed, the constant fragmentation signal produced by the probe laser is depleted. Thus, by scanning the pump laser, a conformer-specific IR-dip spectrum is recorded. IR-dip spectra are corrected for background signal, but are not normalized for laser intensity due to saturation effects.

2.3 Computational methods

Presampling of the potential-energy surface (PES) of LL-/LD-Glu$_2$H$^+$ is accomplished by basin hopping employing the MM3Pro force field as implemented in the TINKER molecular modelling software.[58–61] The 1200 lowest-energy conformers are relaxed at the dispersion-corrected PBE + vdW^{TS}/light density-functional theory (DFT) level.[62,63] Thus, 309 LL and 316 LD conformers are found within $\Delta E \approx 160$ kJ mol^{-1}. All DFT calculations are performed with FHI-aims, which employs numeric atom-centred basis functions for the Kohn–Sham orbitals.[62]

In a second step, the PES of LL-/LD-Glu$_2$H$^+$ is scanned in more detail by replica-exchange molecular dynamics (REMD) simulations at the PBE/light level.[64–66] 12 independent molecular dynamics trajectories of replicas of LL- and LD-Glu$_2$H$^+$ are simultaneously generated at different temperatures. Every 40 fs, neighbouring pairs of replicas are eventually swapped based on a Metropolis criterion. Thus, individual replicas traverse a wide temperature range to overcome barriers, which ensures efficient sampling of the PES. Structures are extracted from the MD trajectories every 40 fs. The resulting conformers are sequentially clustered (*i.e.*, sorted into structural families) using the GROMOS algorithm (cutoff 0.05 nm) as implemented in the GROMACS program.[67,68]

Harmonic vibrational analysis of the most stable conformers of LL- and LD-Glu$_2$H$^+$ is accomplished at the many-body dispersion (MBD) corrected hybrid DFT level PBE0 + MBD/tight.[69] Harmonic frequencies are used to calculate zero-point corrected energies (E_0) and Helmholtz free energies at 15 K (F_{15}) and 300 K (F_{300}).[70] Calculated linear IR absorption spectra are linearly scaled by factors of 0.93 (2600–3600 cm^{-1}) to roughly adjust the experimental free OH stretching vibration (band A1), and 0.955 (1100–1900 cm^{-1}) to adjust the CO stretching vibrations (bands K1–K4).

For the global minimum conformers, the noncovalent interaction (NCI) method is applied.[71] To this end, the reduced gradient of the electron density ($s(\rho) \sim |\mathrm{grad}(\rho)|/\rho^{4/3}$) is evaluated as a function of the electron density ρ to provide a measure of the strengths of the noncovalent interactions.

3. Results and discussion

3.1 Overview IRPD spectroscopy of LL- and LD-Glu$_2$H$^+$

The IRPD spectra of cryogenic LL-/LD-Glu$_2$H$^+$-H$_2$ in the XH stretch and fingerprint ranges are compared in Fig. 1. Peak positions and assignments are listed in Tables S1 and S2 in ESI.† LL- and LD-Glu$_2$H$^+$ clearly show diastereospecific IR signatures with different peak positions and intensities. In the fingerprint range, the NH bending modes δ_{NH_3} (bands N and M) and δ_{NH_2} (band L) and the CO stretches ν_{CO} (bands K1–K4) are sensitive to chirality. In the XH stretch range, the IRPD spectra also differ significantly. For example, LD-Glu$_2$H$^+$ shows a ν_{OH} doublet (bands A1 and A2) in contrast to the single peak of LL-Glu$_2$H$^+$ (A1). These discrepancies result from different conformational landscapes of LL- and LD-Glu$_2$H$^+$ (structure of the conformers, interaction strengths, conformer population). In the following, these stereochemistry-induced effects are disentangled with the aid of IR–IR hole burning spectroscopy, isotope-labelling and quantum chemistry.

3.2 Conformations of LL- and LD-Glu$_2$H$^+$

Relevant LL- and LD-Glu$_2$H$^+$ conformers are depicted in Fig. 2. Additional structures are shown in Fig. S1 and S2 (ESI†). Binding energies (D_0) are derived using the most stable gas-phase monomers, according to $D_0 = E_0(\mathrm{Glu_2H^+}) - E_0(\mathrm{GluH^+}) - E_0(\mathrm{Glu})$.[47,51] The complex energy hierarchy of LL-/LD-Glu$_2$H$^+$ is shown in Fig. 3 (Table S3, ESI†). The most stable LD-Glu$_2$H$^+$ conformer (LD1) is more stable than the most stable LL-Glu$_2$H$^+$ conformer (LL1) by $\Delta E_0 = 4.0$ kJ mol^{-1} (Table S3, ESI†). The energy gap to the respective global minimum is larger for

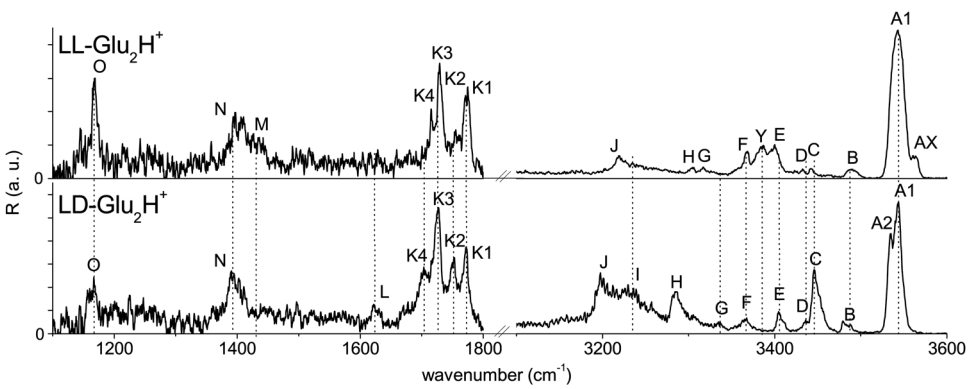

Fig. 1 Overview IRPD spectra of diastereospecific LL- (top) and LD-Glu$_2$H$^+$-H$_2$ (bottom) recorded in the XH stretch (X = O, N; 3100–3600 cm^{-1}) and fingerprint ranges (1100–1900 cm^{-1}). Peak positions and assignments are listed in Tables S1 and S2 in ESI.†

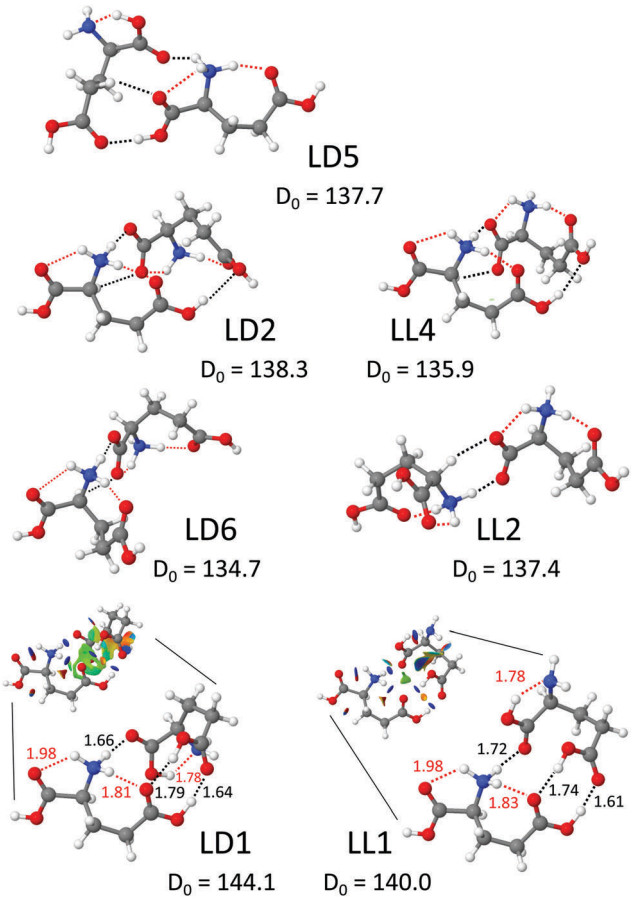

Fig. 2 Relevant structures of LL-/LD-Glu_2H^+ with intramolecular (red) and intermolecular (black) H-bonds. Binding energies (D_0, kJ mol^{-1}) calculated at the PBE0 + MBD/tight level are also given. Corresponding LL and LD structures are drawn next to each other. For the global minima, LD1 and LL1, H-bond lengths (R, Å) and NCI plots are added.

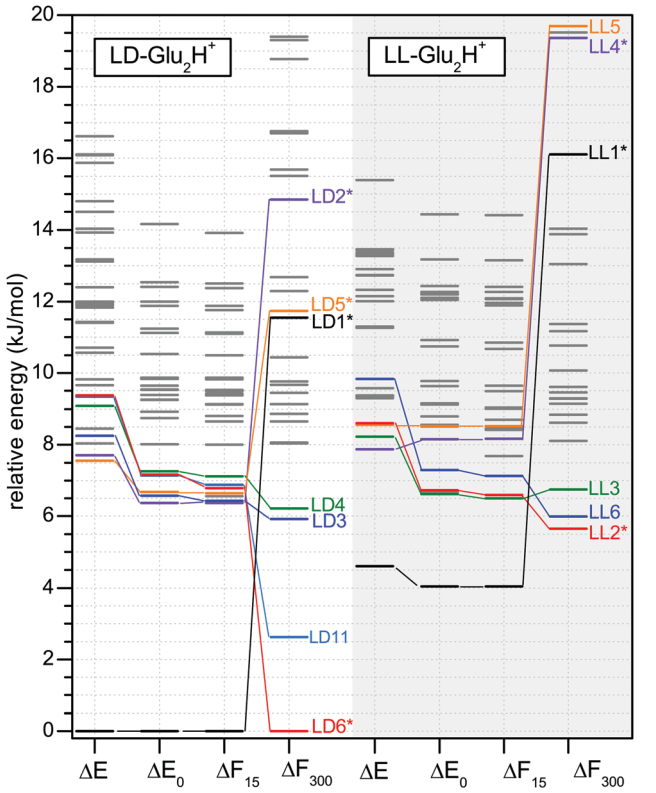

Fig. 3 Energy hierarchy diagram of the most stable LL- and LD-Glu_2H^+ conformers (ΔE < 20 kJ mol^{-1}). Relative zero-point corrected energies (ΔE_0, kJ mol^{-1}), and relative free energies at 15 and 300 K (ΔF_{15} and ΔF_{300}, kJ mol^{-1}) are also given to illustrate temperature effects (Table S3, ESI†). Assigned conformers are marked with asterisks.

LD-Glu_2H^+ (ΔE_0 = 6.4 kJ mol^{-1}) than for LL-Glu_2H^+ (ΔE_0 = 2.7 kJ mol^{-1}). The ions probed are generated at room temperature and subsequently cooled down to 15 K in the QIT. To assess temperature effects, we evaluate relative zero-point corrected energies (ΔE_0) and relative Helmholtz free energies at 15 and 300 K (ΔF_{15} and ΔF_{300}). Indeed, temperature drastically affects the energy hierarchy. Stabilization of certain conformers is likely dominated by the vibrational entropy term, $TS \sim -k_B T \ln(1 - \exp(-\hbar\omega/k_B T))$, which is part of the free energy, $F = E_{PES} + \Delta U - TS$, where E_{PES} is the electronic minimum energy on the PES, ΔU is the harmonic internal energy including zero-point vibrational energy, and TS is the harmonic vibrational entropy term.[72] The logarithm makes low-frequency normal modes dominate the temperature-dependent vibrational entropy term. Inspection of Table S4 and Fig. S3 (ESI†) reveals this correlation for LD3, LD6, LD11, LL2, LL3, and LL6, which benefit most from entropy, because their low frequencies are the smallest. While LD1 and LL1 are the global minima at low temperature (ΔE_0, ΔF_{15}), they are strongly destabilized at room temperature (ΔF_{300} > 11 kJ mol^{-1}). Both, LD1 and LL1 are rather rigid structures with three strong intermolecular H-bonds. Floppy LD6 and LL2 with only two H-bonds connecting their compact subunits are favoured at 300 K. However, the experimental cooling process is regulated by energy barriers separating conformers, which are not mapped by the calculations. Thus, for assigning the experimental spectra, we consider the structures most stable at 15 K and at 300 K.

In general, stabilization of LL- and LD-Glu_2H^+ relies on a balance of intra- and intermolecular H-bonds (*vide infra*). Interestingly, the H-bond networks are very similar in LL- and LD-Glu_2H^+. Corresponding structures mainly differ due to steric constraints imposed by the chirality of the partners. In all LL- and LD-Glu_2H^+ dimers, intramolecular H-bonds (red dotted lines in Fig. 2 and Fig. S1, S2, ESI†) strongly compete with intermolecular H-bonds (black dotted lines). HOCO···HNH···OCOH H-bonds to the NH_3^+ group lock the conformation of $GluH^+$ and zwitterionic Glu, making these subunits very similar to the two previously identified $GluH^+$ monomers.[47,51] Non-zwitterionic neutral Glu is very flexible and adapts to $GluH^+$ (LD1, LD5, LL1).

Although the intra- and intermolecular H-bonds formed in the LD1 and LL1 conformers connect the same groups of the two subunits, LD1 (D_0 = 144.1 kJ mol^{-1}) is tighter bound than LL1 (D_0 = 140.0 kJ mol^{-1}). Comparison of H-bond lengths does not rationalize their relative stability. The strongest H-bonds of LL1 are found within the HO···COOH···OC bridge (R = 1.61/1.74 Å),

whereas these H-bonds are somewhat weaker for LD1 (R = 1.64/1.79 Å). The intermolecular NH···O H-bond is stronger for LD1 (R = 1.66 *vs.* 1.72 Å). To reveal the origin of the enhanced stability of LD1, we performed exemplary NCI calculations for LD1 and LL1 (shown as insets in Fig. 2; NCI plots in Fig. S4, ESI†). Obviously, green and light-blue NCI isosurfaces occur between the two subunits of LD1, representing weak but extended attractive regions. The α-COOH of Glu and the γ-COOH of $GluH^+$ are close in LD1 facilitating this attractive secondary interaction. In contrast, due to steric constraints, LL1 lacks such a stabilizing interaction. Within the NCI approach, the strength of a certain noncovalent interaction is given by the ρ^* value of the respective minimum of the reduced density gradient.[71] Indeed, with $\Sigma(\rho^*)$ = 0.306 a.u. the total attractive interaction in LD1 is larger than in LL1 with 0.289 a.u. Interestingly, comparison of ρ^* values reveals that the stabilization of LD1 predominantly results from stronger H-bonds ($\Sigma(\rho^*)$ = 0.277 *vs.* 0.267 a.u. for LD1 *vs.* LL1), which is not obvious from their geometries (Fig. S4, ESI†). Induction and dispersion are also enhanced ($\Sigma(\rho^*)$ = 0.029 *vs.* 0.022 a.u. for LD1 *vs.* LL1). The IR spectra of LD1 and LL1 (Fig. 4, 5 and Tables S1, S2, ESI†) show one single free OH stretching mode (ν^f_{OH}) predicted at 3530 and 3529 cm^{-1}, respectively. Free antisymmetric and symmetric stretches of the NH_2 group ($\nu^{f(as)}_{NH_2}$ and $\nu^{f(s)}_{NH_2}$) occur at 3409 and 3313 (LD1) or 3413 and 3326 cm^{-1} (LL1). The NH stretching frequencies of the NH_3^+ group of LL1 are red-shifted due to the intramolecular H-bonds ($\nu^b_{NH_3}$). One of them couples to a strongly red-shifted $\nu^b_{\gamma OH}$ of the $(COOH)_2$ ring resulting in an intense doublet at 3161/3147 cm^{-1}. The third NH stretch of NH_3^+ is drastically red-shifted due to the stronger intermolecular H-bond ($<$2800 cm^{-1}). Though the H-bonds in LD1 are comparable to those described for LL1, its respective $\nu^b_{\gamma OH}$ and $\nu^b_{NH_3}$ are not coupled and occur separately at 3223 and 3152 cm^{-1}. In the fingerprint range, the most characteristic features of LL1 and LD1 are their intense δ_{NH_3} and δ_{NH_2} around 1600 cm^{-1}. LD5 (D_0 = 137.7 kJ mol^{-1}) is structurally related to LD1. Its neutral Glu subunit also occurs in the non-zwitterionic form (contrarily to LD2 and LD6). However, the flexible Glu subunit is distorted and the intermolecular H-bonds differ from those in LD1. For example, we do not observe the characteristic $(COOH)_2$ ring occurring in LD1.

LD6 and LL2, most stable at 300 K, are also structural relatives. Both contain a zwitterionic Glu. The COO^- group is involved as H-bond acceptor in three H-bonds: two intermolecular H-bonds with the NH_3^+ and CH groups of $GluH^+$, and one intramolecular H-bond with the NH_3^+ group of the zwitterion. Their binding energies are comparable, D_0 = 134.7 *vs.* 137.4 kJ mol^{-1}. In the range measured, their IR spectra are characterized by a ν^f_{OH} triplet between 3533 and 3536 cm^{-1}, one free NH stretching mode of the NH_3^+ of the zwitterion ($\nu^f_{NH_3}$) around 3330 cm^{-1} and one H-bonded NH stretching mode of NH_3^+ of $GluH^+$ H-bonded to α-COOH ($\nu^b_{NH_3}$) around 3200 cm^{-1}. The impact of the H-bond network on all other NH stretches is so strong that they lie below 3000 cm^{-1}. In the fingerprint range, the existence of one COO^- and three COOH groups results in a specific ν_{CO} pattern. The $\nu_{\alpha CO}$ occurs at 1771–1774 cm^{-1}, the $\nu_{\gamma CO}$ doublet at 1710–1724/1711–1726 cm^{-1}, and the antisymmetric COO^- stretch (ν_{COO-}) at 1656–1654 cm^{-1}. The corresponding symmetric CO stretch of the COO^- group is found at 1379 cm^{-1}. LD2 and LL4 also contain one zwitterionic Glu. The conformation of the protonated subunit is the same as in LL1 and LD1. The additional OH···O contact provokes a characteristic red-shifted $\nu^b_{\gamma OH}$ found at 3512 and 3488 cm^{-1}, respectively.

3.3 IR–IR hole burning spectra in the XH stretch range

In the XH stretch range, transitions H, Y, E, and C (Fig. 1) are the fingerprints of chirality recognition of LL- and LD-Glu_2H^+. Y is observed in the LL-Glu_2H^+ spectrum but absent in the LD-Glu_2H^+ spectrum. At the same time, E undergoes an 8 cm^{-1} blue shift from LL- to LD-Glu_2H^+, while C experiences a strong enhancement. H experiences both a 16 cm^{-1} red shift and an enhancement from LL- to LD-Glu_2H^+. A preliminary assignment of the experimental bands results from ^{15}N isotope-labelling of L-Glu (Fig. S5, ESI†). ^{15}N-Labelling induces a typical red shift of 8 cm^{-1} of ν_{NH} facilitating to distinguish them from ν_{OH}. Thus, we reveal bands AX, A1, B, and Y of LL-Glu_2H^+ as well as A1, A2, and B of LD-Glu_2H^+ as ν_{OH}. All other transitions probed shift to the red upon isotope-labelling and are thus assigned to ν_{NH} modes. However, isotope-labelling cannot disentangle the conformer contribution. Hence, we employ IR–IR hole burning spectroscopy.

Fig. 4 compares the IR–IR hole burning spectra of LL-/LD-Glu_2H^+ to the scaled (0.93) linear IR absorption spectra of the assigned conformers calculated at the PBE0 + MBD/tight level (see also Fig. S6 and S7, ESI†). Peak positions and assignments are listed in Table S1 (ESI†). Calculated spectra of additional low-energy conformers are shown in Fig. S8 (ESI†). Setting the probe laser at the most intense features of its IRPD spectrum (3368, 3397, and 3487 cm^{-1}), three conformers of LL-Glu_2H^+ are found. Four conformers of LD-Glu_2H^+ are detected with the probe laser set at 3367, 3405, 3445, and 3486 cm^{-1}. All transitions present in the IRPD spectra are thus burnt, indicating that (at least) the dominant conformers are found.

Comparison of band positions of the four IR-dip spectra of LD-Glu_2H^+ indicates that the spectra probed at 3445, 3367, and 3405 cm^{-1} are contaminated (by each other). Such a contamination may result from probing overlapping IRPD bands. In the present case, it is more likely related to the RF tickling. The tickling frequency depends on m/z of the ion to be ejected from the QIT. Apparently, the choice of the tickling frequency is slightly off from the optimal value for the LD dimers. Hence, either the m/z range for ejection is not sufficiently narrow causing ejection also of some intact parent clusters, or many collisions are provoked upon tickling resulting in strong collision-induced dissociation (CID) of intact parent clusters. Some weak features can thus be assigned to contamination as indicated by crosses in Fig. 4. Neglecting the contamination bands, the LD-Glu_2H^+ IR-dip spectra compare well to those measured for LL-Glu_2H^+. Indeed, we find a compelling correspondence between the IR-dip spectra of LL- and LD-Glu_2H^+, that are drawn abreast in Fig. 4.

Assignment of the IR-dip spectra to calculated conformers is based on (i) stability and (ii) agreement of measured and

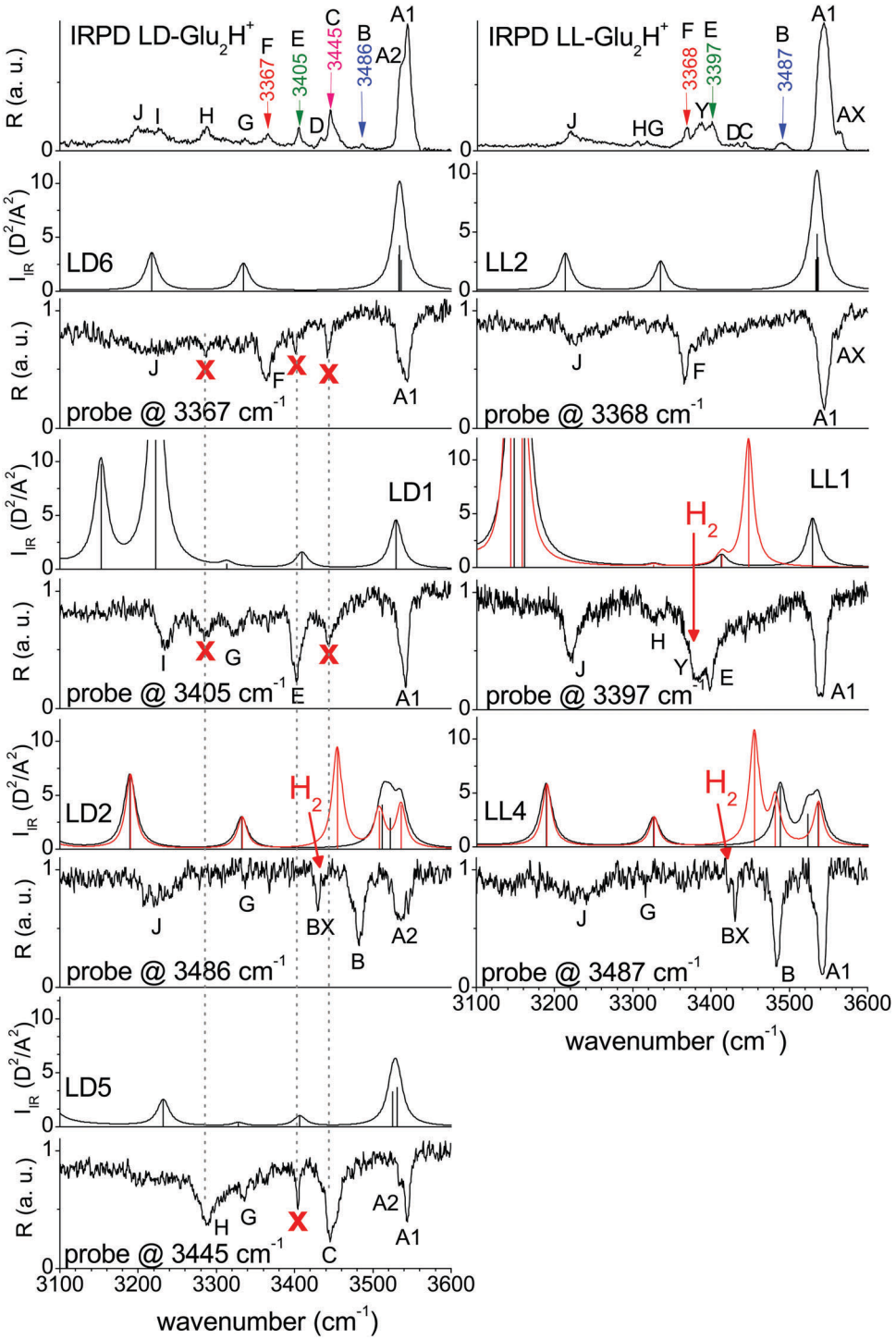

Fig. 4 IRPD and IR–IR hole burning spectra of LL-/LD-Glu_2H^+-H_2 recorded in the XH stretch range (X = O, N; 3100–3600 cm^{-1}) compared to calculated IR absorption spectra of the assigned conformers (stick spectra and convolution with Lorentzian profile, FWHM 8 cm^{-1}). Left: Four dominant conformers of LD-Glu_2H^+ probed at 3445, 3486, 3405, and 3367 cm^{-1}. Right: Three dominant conformers of LL-Glu_2H^+ probed at 3487, 3397, and 3368 cm^{-1} as indicated by arrows in the IRPD spectrum. Red traces correspond to calculated H_2-tagged conformers (Fig. S8–S12, ESI†). The red crosses indicate contamination bands, which are not considered for assignment.

calculated IR spectra. To check for discrepancies between different levels of theory, the spectra of the most stable conformers found by REMD are recalculated also at the B3LYP/cc-pVTZ and PBE0/cc-pVTZ levels (Fig. S9, ESI†).

After cancelling the contamination bands, the IR-dip spectrum of LD-Glu_2H^+ probed at 3367 cm^{-1} contains two well-resolved peaks at 3542 (A1) and 3365 (F) cm^{-1} and a broad band around 3200 cm^{-1} (J). Band A1 is readily assigned to a free

OH stretching mode (ν^{f}_{OH}). Bands F and J are unmasked as NH stretching modes by ^{15}N-labelling. Conformers that comprise two NH_3^+ groups are candidates to explain this IR pattern. The IR absorption spectrum calculated for the most stable conformer at room temperature, LD6, matches well. We assign band F at 3365 cm^{-1} to its $\nu^{f}_{NH_3}$ predicted at 3334 cm^{-1} and band J at around 3200 cm^{-1} to its $\nu^{b}_{NH_3}$ predicted at 3217 cm^{-1}.

The second IR-dip spectrum of LD-Glu_2H^+ probed at 3405 cm^{-1} shows four bands at 3542 (A1), 3402 (E), 3325 (G), and 3238 (I) cm^{-1}. Band E is a characteristic of a free NH_2 group that is found in the low-temperature global minimum LD1. Due to stability and the moderate match of predicted and measured spectra we assign LD1. Band A1 is its ν^{f}_{OH} calculated at 3530 cm^{-1}, E and G are its antisymmetric and symmetric NH_2 stretches ($\nu^{f(as)}_{NH_2}$ and $\nu^{f(s)}_{NH_2}$) predicted at 3409 and 3313 cm^{-1}. The assignment of I is not straightforward, because the measured IR intensity is rather low compared to any of the predicted transitions in that frequency range. However, IR-dip spectra are not normalized for laser power variation, and the hole burning IR intensities are not entirely reliable due to saturation effects. As transition I in the IRPD spectrum shifts upon ^{15}N-labelling, we tend to assign it to a ν_{NH}. Hence, we tentatively assign it to $\nu^{b}_{NH_3}$ predicted at 3152 cm^{-1}. The most intense calculated peak here, $\nu^{b}_{\gamma OH}$ of LD1 predicted with an enormous IR intensity of 26.6 D^2/A^2 at 3223 cm^{-1}, is thus probably contained in the broad absorption background below 3200 cm^{-1} (Fig. S6 and S7, ESI†).

The third spectrum probed at 3486 cm^{-1} (band B) is dominated by an intense triplet at 3536 (A2), 3483 (B), and 3430 (BX) cm^{-1} and a broad band around 3200 cm^{-1} (J). From ^{15}N-labelling, A2 and B are clearly assigned to ν_{OH}. A2 can readily be distinguished as ν^{f}_{OH} and B as ν^{b}_{OH}. As already mentioned in Section 3.2, among the most stable structures, only LD2 has a weakly bound OH group, that gives rise to a slightly red-shifted ν^{b}_{OH}. Its predicted IR spectrum closely resembles the measured IR-dip spectrum except for the least intense band BX. However, it can be explained considering H_2-tagging. Attachment of H_2 at the free OH groups of $GluH^+$ or Glu leads to conformers LD2-H_2(OH1) and LD2-H_2(OH3), respectively (Fig. S10, ESI†). The H_2 tag is bound by D_0 = 0.82 and 0.86 kJ mol^{-1}. A somewhat less stable binding motif (D_0 = 0.71 kJ mol^{-1}) results from insertion of H_2 into the intermolecular OH···O bond between $GluH^+$ and Glu, LD2-H_2(OH2). Corresponding IR spectra are shown in Fig. S11 (ESI†). Indeed, band BX can be rationalized by the red-shifted ν^{f}_{OH} of LD2-H_2(OH1) predicted at 3508 cm^{-1}. Yet, also LD2-H_2(OH2) and LD2-H_2(OH3) may contribute to the IR-dip spectrum (Fig. S11, ESI†). Finally, the triplet is readily reproduced by superimposing the spectra of LD2 and LD2-H_2(OH1). Band J observed near 3200 cm^{-1} is assigned to $\nu^{b}_{NH_3}$ of LD2 predicted at 3190 cm^{-1}.

The fourth IR-dip spectrum measured with the probe laser set at 3445 cm^{-1} (band C) is the only LD spectrum without LL analogue. It shows a doublet A1/A2 in the ν^{f}_{OH} range at 3544 and 3535 cm^{-1}, and two intense bands at 3446 (C) and 3290 (H) cm^{-1}. Band C is characteristic of a free NH_2 group, contained in LD5, for example. Furthermore, in the spectrum of LD5, two distinct ν^{f}_{OH} occur at 3531 and 3526 cm^{-1}, which are assigned to A1 and A2, respectively. Consequently, band C is attributed to $\nu^{f(as)}_{NH_2}$ of LD5, predicted somewhat low at 3407 cm^{-1}, and band H corresponds to $\nu^{b}_{NH_3}$. Its $\nu^{f(s)}_{NH_2}$ may be found as a small shoulder G at 3336 cm^{-1}.

Finally, all four IR-dip spectra of LD-Glu_2H^+ are readily assigned to low-energy isomers at 15 K (LD1 and LD5) or at 300 K (LD2 and LD6). Thus, we find a mixture of cooling processes in the QIT. Complete thermalization leads to population of the global minima at the temperature of the trap. Kinetic trapping resulting from high potential barriers prevents conformational changes during the cooling process. The intensity distribution in the IRPD spectrum indicates a predominant production of the low temperature minima LD1 and LD5. Band C, a fingerprint of LD5, and band E, characteristic of LD1, are intense. Band B is less intense, revealing a minor population of LD2. LD6 probed at 3367 cm^{-1} seems also less abundant than LD5 and LD1. Conformers LD11, LD3, and LD4 that are rather stable at 300 K (Fig. 3) have almost the same IR spectra as LD6 (Fig. S8, ESI†) in the range probed. They are ruled out based on stability.

The three IR-dip spectra of LL-Glu_2H^+ are not contaminated. The spectrum obtained with the probe laser set at 3368 cm^{-1} shows four peaks at 3565, 3544, 3365, and 3226 cm^{-1} that correspond to bands AX, A1, F, and J in the IRPD spectrum. Considering the lowest energy isomers at 15 and 300 K, the spectrum is best reproduced by conformer LL2 (see also Fig. S8, ESI†). Its similarity to the IR-dip spectrum of LD-Glu_2H^+ probed at 3367 cm^{-1} is obvious. It is assigned to LD6, which is structurally closely related to LL2, supporting this assignment. Hence, we assign AX and A1 to ν^{f}_{OH} of LL2 predicted at 3536, 3534, and 3533 cm^{-1}, F to $\nu^{f}_{NH_3}$ at 3335 cm^{-1} and J to $\nu^{b}_{NH_3}$ at 3231 cm^{-1} (Table S1, ESI†).

The IR-dip spectrum probed at 3397 cm^{-1} shows four intense peaks at 3541 (A1), 3398 (E), 3383 (Y), and 3223 (J) cm^{-1}. A1 is readily assigned to ν^{f}_{OH}, but is not conformer-specific. Band E is characteristic of a free NH_2 group ($\nu^{f}_{NH_2}$), whereas J can be assigned to a bound NH_3 group ($\nu^{b}_{NH_3}$). Therefore, we tend to assign the low-temperature global minimum LL1, although the match of its calculated IR spectrum is not perfect. Band Y has already been verified as ν_{OH} by isotope-labelling. To assign band Y, we consider H_2-tagging of LL1 at its free OH group (Fig. S10, ESI†), whose ν_{OH} is drastically red-shifted upon H_2 attachment (Fig. S12, ESI†). Hence, we assign band Y at 3381 cm^{-1} to ν^{b}_{OH} of LL1-H_2(OH), while its red shift is somewhat underestimated (predicted at 3447 cm^{-1}). Except for band Y, the IR-dip spectrum probed at 3397 cm^{-1} (band E) resembles that of LD-Glu_2H^+ probed at 3405 cm^{-1} that is attributed to LD1. LD1 and LL1 have a related conformation with similar intra- and intermolecular H-bonds. Again, this similarity supports our assignment.

The IR-dip spectrum of LL-Glu_2H^+ probed at 3487 cm^{-1} resembles that of LD-Glu_2H^+ probed at 3486 cm^{-1}. A similar triplet occurs at 3543 (A1), 3484 (B), and 3431 cm^{-1}. In analogy, it is assigned to ν^{f}_{OH} and ν^{b}_{OH} of LL4 predicted at 3536/3523 and 3488 cm^{-1} and the H-bonded ν^{b}_{OH} of LL4-H_2(OH1) predicted at 3481. With D_0 = 1.15 kJ mol^{-1}, LL4-H_2(OH1) is the

most stable H_2-tagged conformer (Fig. S10, ESI†). However, the IR spectra of LL4-H_2(OH2) and LL4-H_2(OH3) (Fig. S13, ESI†) can also explain the observed triplet. Hence, we assume a superposition of all three H_2-tagged conformers, with LL4-H_2(OH1) as the dominant conformer in the trap. The triplet is not clearly visible in the IRPD spectrum of LL-Glu$_2$H$^+$, but may be contained in the unresolved range between bands B and C.

Band B is significantly less intense than E or F revealing a minor production of conformer LL4. The IRPD spectrum suggests the predominant population of LL1 because bands E and Y are intense. LL2 may however be as abundant as LL1. Band F, assigned to LL2, is only somewhat less intense than E or Y, in line with their lower predicted IR intensity of ν^{f}_{NH} relative to ν^{f}_{OH}. The IR spectra of conformers LL6 and LL3, that are stabilized by entropy at 300 K (Fig. 3), are very similar to that of LL2 (Fig. S8, ESI†). Due to their lower stability, however, they are not considered for assignment.

Finally, the IRPD spectrum of LD-Glu$_2$H$^+$ can be rationalized by LD1, LD2, LD5, and LD6, which are among the most stable conformers at room temperature and at 15 K ($\Delta E_0 < 7.0$ kJ mol^{-1}). The IRPD spectrum of LL-Glu$_2$H$^+$ can be explained as a superposition of the spectra of at least LL1, LL2, and LL4 ($\Delta E_0 <$ 4.5 kJ mol^{-1}). Population of additional conformers is however possible. First, we probed only prominent bands to yield sufficient fragmentation signal. Second, only well-resolved bands can be probed by IR–IR hole burning. If bands lie too close or overlap, conformer separation is no longer possible.

3.4 IRPD spectra in the fingerprint range

Fig. 5 compares IRPD spectra of LL-/LD-Glu$_2$H$^+$ in the fingerprint range to the scaled (0.955) linear IR absorption spectra of the assigned conformers (Table S2, ESI†). Fig. S14 (ESI†) shows the IRPD spectra considering the effect of deuteration, along with infrared multiple-photon dissociation (IRMPD) spectra. Further calculated IR spectra are shown in Fig. S15 (ESI†). An assignment of the fingerprint modes is ambiguous because the calculated spectra are rich and similar for the different conformers. This observation emphasizes the importance of measuring both spectral ranges, especially because the XH stretching modes are very sensitive to H-bonds. However, the fingerprint modes confirm the above assignments as follows.

The IRPD spectrum of LD-Glu$_2$H$^+$ supports the assignment of conformers LD1, LD2, LD5, and LD6. Band K1 at 1774 cm^{-1} is assigned to a superposition of $\nu_{\alpha CO}$ of LD1, LD2, and LD6 predicted between 1774 and 1779 cm^{-1}. K2 at 1751 cm^{-1} is composed of $\nu_{\gamma CO}$ of LD-1 and $\nu_{\alpha CO}$ and $\nu_{\gamma CO}$ of LD5 predicted at 1735, 1754, and 1743 cm^{-1}, respectively. K3 at 1728 cm^{-1} arises from $\nu_{\gamma CO}$ of LD2, LD5, and LD6. K4 at 1715 cm^{-1} is somewhat broadened compared to LL-Glu$_2$H$^+$ and is assigned to $\nu_{\gamma CO}$ of LD6 and LD1 at 1710 and 1697 cm^{-1}. Peak L at 1619 cm^{-1} is characteristic of δ_{NH_2} of LD1 and ν_{COO^-} of LD6 predicted at 1619 and 1656 cm^{-1}, respectively. Band N is assigned to the NH_3^+ umbrella mode ($\delta^{u}_{NH_3}$) of LD2 and LD6 superimposed by δ_{OH} of LD1 and LD5. Transition O at 1165 cm^{-1} is a superposition of δ^{f}_{OH} of all conformers (Table S2, ESI†).

The IRPD spectrum of LL-Glu$_2$H$^+$ supports the assignment of conformers LL1, LL2, and LL4. K1 at 1774 cm^{-1} is assigned to a superposition of $\nu_{\alpha CO}$ of LL1, LL2, and LL4 predicted between 1771 and 1779 cm^{-1}. K2 at 1751 cm^{-1} is attributed to $\nu_{\gamma CO}$ of LL2 somewhat underestimated at 1726 cm^{-1}. K3 at 1728 cm^{-1} is $\nu_{\gamma CO}$ of LL1 and LL2 predicted at 1737 and 1732 cm^{-1}, respectively. K4 at 1715 cm^{-1} may be assigned to LL2. The broad intense band M/N at 1432/1400 cm^{-1} arises from $\delta^{u}_{NH_3}$. M is assigned to LL1 (1485/1461 cm^{-1}), N to LL2 (1417 cm^{-1}) and LL4 (1414 cm^{-1}) with some contribution of δ^{b}_{OH} of LL1 (1406 cm^{-1}). Transition O at 1167 cm^{-1} is a superposition of δ^{f}_{OH}.

Especially the ν_{CO} quartet (K1–K4) is sensitive to conformation and relative chirality. The intensity distribution over K1–K4 differs for LD- and LL-Glu$_2$H$^+$. K2 is more intense for LD than LL. Furthermore, the doublet K3/K4 is broadened in LD-Glu$_2$H$^+$. This indicates the coexistence of several conformers and different population ratios.

Apparently, the spectral resolution is enhanced for IRPD compared to IRMPD (dotted lines in Fig. S14, ESI†). Moreover, we observe blue shifts of the IRMPD bands, which are maximal ($\Delta\nu \approx 30$ cm^{-1}) in the ν_{CO} range (K1–K5). Some bands present in the IRPD spectra (L, M) do not occur in the IRMPD spectra, probably due to mode-specific thresholds of the multiple-photon dissociation. By H_2-tagging and cryogenic cooling, single-photon conditions are assured in the IRPD process. Anyway, the overall structure of the IRMPD spectra is similar to that of the corresponding IRPD spectra.

3.5 Chirality recognition of LL- and LD-Glu$_2$H$^+$

Herein, we study the chirality recognition of LL- and LD-Glu$_2$H$^+$ that would be the prerequisite for a potential asymmetric amplification scheme in these prototypical amino acid dimers. Indeed, we find an asymmetry of the relative stability in favour of heterochiral LD-Glu$_2$H$^+$. LD1 is more stable than LL1 by $\Delta E_0 = \Delta D_0 = 4.0$ kJ mol^{-1}, and LD6 is more stable than LL2 by $\Delta F_{300} = 5.6$ kJ mol^{-1} (Table S3, ESI†). This exceeds the observed energy difference in favour of homochiral LL-Ser$_2$H$^+$ of $\Delta G = 0.49$ kJ mol^{-1}.[39] However, our mass spectra do not indicate any clear preference for the heterochiral dimer (Fig. S16, ESI†). Yet, to experimentally verify the stability prediction, we performed CID in the QIT (Fig. 6 and Fig. S17, ESI†). Steadily increasing the RF voltage of the QIT, the trapped ions start to move and collide inside the trap. The higher the RF voltage applied, the higher the collision energy that eventually leads to fragmentation of the cluster. We monitor the fragments of trapped LD- or LL-Glu$_2$H$^+$ as a function of the RF voltage. Fig. 6 shows that LL-Glu$_2$H$^+$ dissociates at 515 V and LD-Glu$_2$H$^+$ at 555 V, in line with a lower binding energy of LL. The kinetic energy of the trapped ions as a function of the RF voltage has been simulated with SIMION[73] (RF frequency: 1 MHz; trapping time: 20 μs; pressure: 4×10^{-5} Torr). This simulation correlates the measured voltages of 515 and 555 V to kinetic energies of approximately 0.16 ± 0.1 and 0.27 ± 0.15 eV with respect to the laboratory frame, respectively. NCI calculations

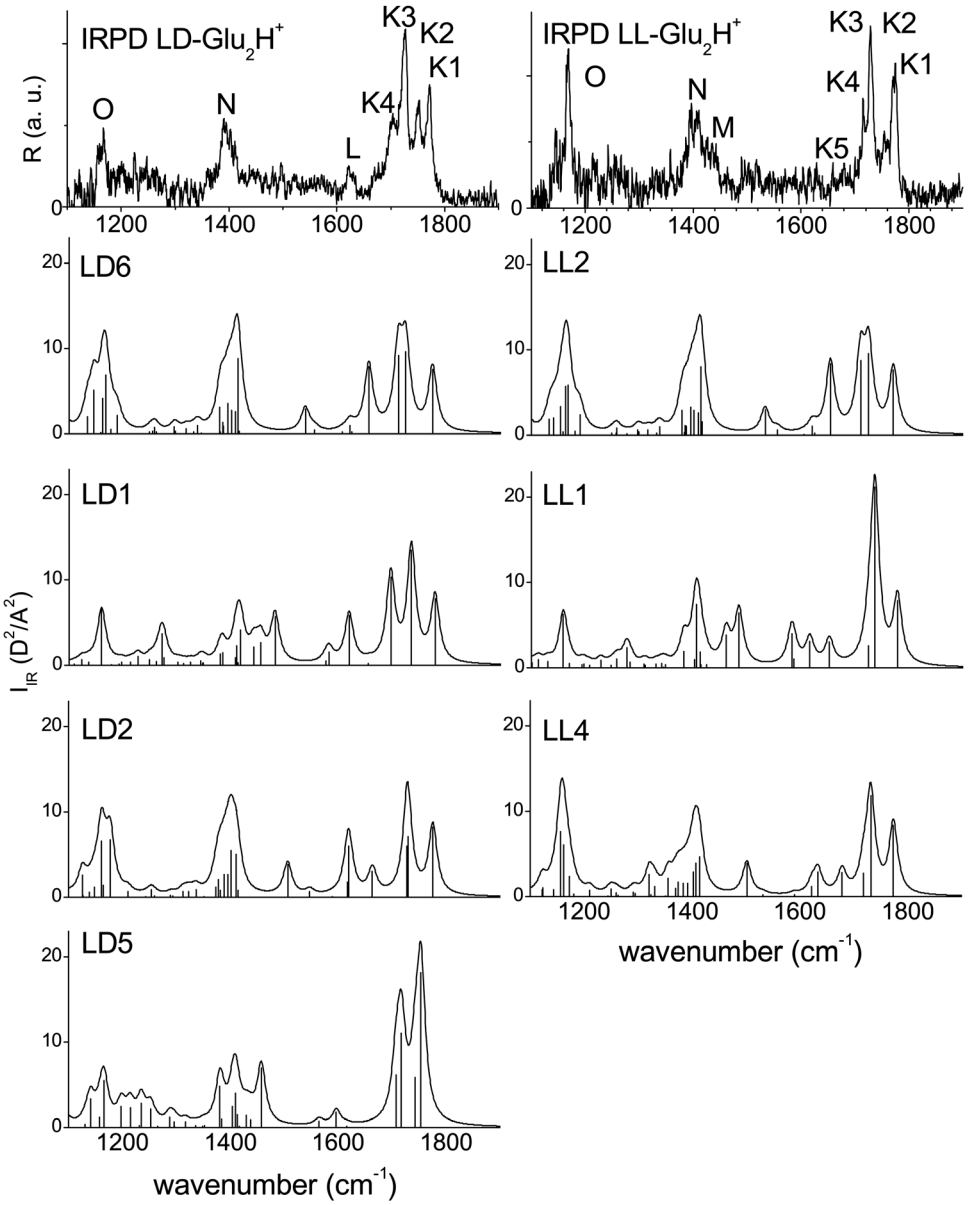

Fig. 5 IRPD spectra of cryogenic LL-/LD-Glu_2H^+-H_2 recorded in the fingerprint range (1100–1900 cm^{-1}) compared to the scaled (0.955) linear IR absorption spectra (stick spectra and convolution with Lorentzian profile, FWHM 10 cm^{-1}) of the assigned conformers calculated at the PBE0 + MBD/tight level.

show that the H-bonds are slightly stronger in LD1 than in LL1. Moreover, due to chirality constraints, LD1 is more compact which promotes the secondary interaction between the α-COOH of Glu and the γ-COOH of $GluH^+$ (Fig. 2 and Fig. S4, ESI†). Hence, chirality recognition of LL- and LD-Glu_2H^+ relies on subtle differences in their H-bond network as well as on secondary interactions optimized in LD rather than LL. LD1 is furthermore distinguished by the gap to less stable conformers. This gap marks the minimal energy necessary to hop from LD1 to another minimum and is most likely even enhanced by isomerization barriers.

Clusters of the amino acid Ser show a remarkable preference for homochirality and are used as prototypical systems to study chirality recognition phenomena possibly relevant in prebiotic chemistry.[32–34] Indeed, we observe stereospecificity of the probed LL- and LD-Glu_2H^+ clusters (IRPD spectra, conformer population, stability). However, there are significant differences between Glu and Ser clusters, worthwhile to be highlighted in order to understand the stereoselectivity of such amino acid clusters. Similar to Glu, L-/D-Ser(H^+) has three functional groups (COOH, OH, and NH_2 or NH_3^+). *Via* three-point interaction, these functional groups are incorporated into stereospecific binding motifs with an interacting partner.[35] This three-point interaction is found to be sensitive to stereochemistry. However, a comparably selective three-point interaction is not possible in LL- and LD-Glu_2H^+ for two main reasons. First, as its backbone is longer, Glu is more flexible than Ser. Therefore, it may adapt somewhat easier to its interacting partner. Second,

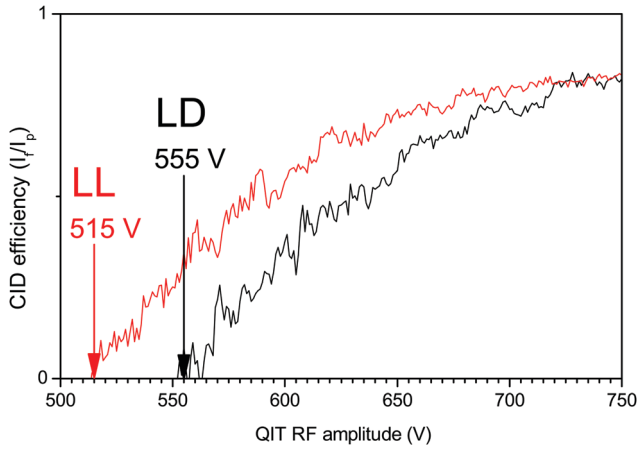

Fig. 6 Collision-induced dissociation (CID) efficiency of LL-/LD-Glu_2H^+ as a function of the RF amplitude of the QIT.

two of the three functional groups of Glu are effectively equal when interacting with a (chiral) partner. L-/D-Glu(H^+) comprise one amino group (NH_2 or NH_3^+) and two almost identical carboxylic groups (α-COOH, γ-COOH). These ideas are in line with the finding that both, the naturally-occurring neurotransmitter L-Glu and its mirror image D-Glu, have excitatory activity, *i.e.*, Glu receptors are less enantioselective.[24]

4. Conclusions

Herein, we report IRPD and IR–IR hole burning spectra of cryogenic LL-/LD-Glu_2H^+ ions in the fingerprint and XH stretch ranges to disentangle the interactions responsible for chirality recognition in these prototypical amino acid dimers. The PES of LL-/LD-Glu_2H^+ is sampled using REMD simulations. The assignment of the IRPD spectra is experimentally aided by ^{15}N-labelling. IR–IR hole burning spectroscopy reveals the coexistence of four LD-Glu_2H^+ and three LL-Glu_2H^+ conformers that are assigned by comparison to calculated IR absorption spectra. The assigned conformers correspond to the most stable conformers at room and cryogenic temperature, revealing incomplete thermalization by kinetic trapping of the ions in the cold trap. Comparing the global minima LD1 and LL1, heterochiral LD-Glu_2H^+ are calculated to be more stable (ΔE_0 = 4.0 kJ mol^{-1}) than homochiral LL-Glu_2H^+. The energy gap above the global minimum is larger for LD-Glu_2H^+ (ΔE_0 = 6.4 kJ mol^{-1}) than for LL-Glu_2H^+ conformers (ΔE_0 = 2.7 kJ mol^{-1}). Collision-induced dissociation of LL-/LD-Glu_2H^+ trapped in the cryogenic quadrupole is consistent with this prediction. This enhanced stability of LD-Glu_2H^+ relies on slightly stronger H-bonds and enhanced dispersion and secondary interactions possible only in LD1 as visualized by NCI plots. Different population ratios result for LL- and LD-Glu_2H^+ conformer, which directly influences their IRPD spectra. In both measured ranges, the spectra show chirality-related characteristics. Particularly, specific ν_{NH_2} ($\approx$3450 cm^{-1}) and ν_{CO} ($\approx$1750 cm^{-1}) modes are fingerprints of chirality recognition. For LD-Glu_2H^+, we find a prominent contribution of the two most stable conformers at 15 K, whereas all three LL-Glu_2H^+ conformers are rather equally abundant. Due to its long backbone, the Glu subunit easily adapts to its interacting partner (here $GluH^+$) such that dimer formation is not very much restricted by stereochemistry.

Conflicts of interest

There are no conflicts to declare.

Acknowledgements

This study was supported by Deutsche Forschungsgemeinschaft (DO 729/3-3). The research leading to part of these results has received funding from the European Union's Seventh Framework Program (FP7/2012-2015) under grant agreement no. 312284 (CLIO project IC 14-019). We thank J.M. Ortega and the CLIO team for valuable support. A. B. thanks the Japan Society for the Promotion of Science for the funding of a Postdoctoral Fellowship for Overseas Researchers (grant no. P16035). J. K. is grateful for a fellowship of the Studienstiftung des deutschen Volkes. The work at Tokyo Institute of Technology is supported by a Grant-in-Aid for Scientific Research KAKENHI on Innovative Area (2503) "Studying the Function of Soft Molecular Systems by the Concerted Use of Theory and Experiment", KAKENHI in the priority area "Molecular Science for Supra Functional Systems", a Grant-in-Aid for Young Scientists KAKENHI, the Cooperative Research Program of "Network Joint Research Center for Materials and Devices", from the Ministry of Education, Culture, Sports, Science and Technology (MEXT), Japan, and the Core-to-Core Program 22003 from the Japan Society for the Promotion of Science (JSPS). O. D. acknowledges travel support from the World Research Hub Initiative (WRHI) of Tokyo Institute of Technology. J. K. and C. B. are grateful to Matthias Scheffler (FHI Berlin) for continuous support of their work.

References

1 S. F. Mason, Biomolecular handedness: origins and significance, *Biochem. Pharmacol.*, 1988, **37**, 1–7.
2 J. L. Bada, Origins of homochirality, *Nature*, 1995, **374**, 594.
3 D. G. Blackmond, The Origin of Biological Homochirality, *Cold Spring Harbor Perspect. Biol.*, 2010, **2**, 1–17.
4 R. Breslow, A likely possible origin of homochirality in amino acids and sugars on prebiotic earth, *Tetrahedron*, 2011, **52**, 2028–2032.
5 R. Breslow and Z.-L. Cheng, On the origin of terrestrial homochirality for nucleosides and amino acids, *Proc. Natl. Acad. Sci. U. S. A.*, 2009, **106**, 9144–9146.
6 K. Ruiz-Mirazo, C. Briones and A. de. La Escosura, Prebiotic Systems Chemistry: New Perspectives for the Origins of Life, *Chem. Rev.*, 2014, **114**, 285–366.
7 M. Quack, J. Stohner and M. Willeke, High-Resolution Spectroscopic Studies and Theory of Parity Violation in Chiral Molecules, *Annu. Rev. Phys. Chem.*, 2008, **59**, 741–769.

8 C. Stoeffler, B. Darquié, A. Shelkovnikov, C. Daussy, A. Amy-Klein, C. Chardonnet, L. Guy, J. Crassous, T. R. Huet and P. Soulard, *et al.*, High resolution spectroscopy of methyltrioxorhenium: towards the observation of parity violation in chiral molecules, *Phys. Chem. Chem. Phys.*, 2011, **13**, 854–863.

9 J. R. Cronin and S. Pizzarello, Enantiomeric Excesses in Meteoritic Amino Acids, *Science*, 1997, **275**, 951.

10 I. Myrgorodska, C. Meinert, Z. Martins, L. Le Sergeant d'Hendecourt and U. J. Meierhenrich, Molecular Chirality in Meteorites and Interstellar Ices, and the Chirality Experiment on Board the ESA Cometary Rosetta Mission, *Angew. Chem., Int. Ed.*, 2014, **54**, 1402–1412.

11 J. J. Flores, W. A. Bonner and G. A. Massey, Asymmetric photolysis of (RS)-leucine with circularly polarized ultraviolet light, *J. Am. Chem. Soc.*, 1977, **99**, 3622–3625.

12 P. Marcellus, M. Nuevo, G. Danger, D. Deboffle, L. d'Hendecourt, C. Meinert, J.-J. Filippi, L. Nahon and U. J. Meierhenrich, Non-racemic Amino Acid Production by Ultraviolet Irradiation of Achiral Interstellar Ice Analogues with Circular Polarized Light, *Astrophys. J., Lett.*, 2011, **727**, 1–6.

13 T. Shibata, J. Yamamoto, N. Matsumoto, S. Yonekubo, S. Osanai and K. Soai, Amplification of a Slight Enantiomeric Imbalance in Molecules Based on Asymmetric Autocatalysis: The First Correlation between High Enantiomeric Enrichment in a Chiral Molecule and Circularly Polarized Light, *J. Am. Chem. Soc.*, 1998, **120**, 12157–12158.

14 M. Klussmann, H. Iwamura, S. P. Mathew, D. H. Wells Jr, U. Pandya, A. Armstrong and D. G. Blackmond, Thermodynamic control of asymmetric amplification in amino acid catalysis, *Nature*, 2006, **441**, 621–623.

15 K. Soai, T. Shibata, H. Morioka and K. Choji, Asymmetric autocatalysis and amplification of enantiomeric excess of a chiral molecule, *Nature*, 1995, **378**, 767–768.

16 I. Sato, H. Urabe, S. Ishiguro, T. Shibata and K. Soai, Amplification of Chirality from Extremely Low to Greater than 99.5% ee by Asymmetric Autocatalysis, *Angew. Chem., Int. Ed.*, 2003, **42**, 315–317.

17 K. Hamase, A. Morikawa and K. Zaitsu, D-Amino acids in mammals and their diagnostic value, *J. Chromatogr. B: Anal. Technol. Biomed. Life Sci.*, 2002, **781**, 73–91.

18 Y. Kera, H. Aoyama, H. Matsumura, A. Hasegawa, H. Nagasaki and R. Yamada, Presence of free D-glutamate and D-aspartate in rat tissues, *Biochim. Biophys. Acta*, 1995, **1243**, 282–286.

19 S. R. Platt, The role of glutamate in central nervous system health and disease – a review, *Vet. J.*, 2007, **173**, 278–286.

20 G. Riedel, B. Platt and J. Micheau, Glutamate receptor function in learning and memory, *Behav. Brain Res.*, 2003, **140**, 1–47.

21 H. Tapiero, G. Mathé, P. Couvreur and K. Tew II, Glutamine and glutamate, *Biomed. Pharmacother.*, 2002, **56**, 446–457.

22 B. S. Meldrum, Glutamate as a Neurotransmitter in the Brain: Review of Physiology and Pathology, *J. Nutr.*, 2000, **130**, 1007–1015.

23 S. Garattini, Glutamic Acid, Twenty Years Later, *J. Nutr.*, 2000, **130**, 901–909.

24 A. M. Benjamin and J. H. Quastel, Cerebral Uptakes and Exchange Diffusion in Vitro of L- and D-Glutamates, *J. Neurochem.*, 1976, **26**, 431–441.

25 N. C. Danbolt, Glutamate uptake, *Prog. Neurobiol.*, 2001, **65**, 1–105.

26 A. Zehnacker and M. A. Suhm, Chirality Recognition between Neutral Molecules in the Gas Phase, *Angew. Chem., Int. Ed.*, 2008, **47**, 6970–6992.

27 D. Scuderi, K. Le Barbu-Debus and A. Zehnacker, The role of weak hydrogen bonds in chiral recognition, *Phys. Chem. Chem. Phys.*, 2011, **13**, 17916–17929.

28 J. Altnoder, A. Bouchet, J. J. Lee, K. E. Otto, M. A. Suhm and A. Zehnacker-Rentien, Chirality-dependent balance between hydrogen bonding and London dispersion in isolated (+/−)-1-indanol clusters, *Phys. Chem. Chem. Phys.*, 2013, **15**, 10167–10180.

29 M. Speranza, F. Rondino, M. Satta, A. Paladini, A. Giardini, D. Catone and S. Piccirillo, Molecular and supramolecular chirality: R2PI spectroscopy as a tool for the gas-phase recognition of chiral systems of biological interest, *Chirality*, 2009, **21**, 119–144.

30 T. D. Veenstra, Electrospray ionization mass spectrometry in the study of biomolecular non-covalent interactions, *Biophys. Chem.*, 1999, **79**, 63–79.

31 A. B. Costa and R. G. Cooks, Origin of chiral selectivity in gas-phase serine tetramers, *Phys. Chem. Chem. Phys.*, 2011, **13**, 877–885.

32 R. G. Cooks, D. Zhang, K. J. Koch, F. C. Gozzo and M. N. Eberlin, Chiroselective Self-Directed Octamerization of Serine: Implications for Homochirogenesis, *Anal. Chem.*, 2001, **73**, 3646–3655.

33 K. J. Koch, F. C. Gozzo, D. Zhang, M. N. Eberlin and R. G. Cooks, Serine octamer metaclusters: formation, structure elucidation and implications for homochiral polymerization, *Chem. Commun.*, 2001, 1854–1855.

34 Z. Takats, S. C. Nanita and R. G. Cooks, Serine Octamer Reactions: Indicators of Prebiotic Relevance, *Angew. Chem., Int. Ed.*, 2003, **42**, 3521–3523.

35 V. Scutelnic, M. A. S. Perez, M. Marianski, S. Warnke, A. Gregor, U. Rothlisberger, M. T. Bowers, C. Baldauf, G. Helden and T. R. von; Rizzo, *et al.*, The Structure of the Protonated Serine Octamer, *J. Am. Chem. Soc.*, 2018, **140**, 7554–7560.

36 F. Pollreisz, Á. Gömöry, G. Schlosser, K. Vékey, I. Solt and G. C. Attila, Mass Spectrometric and Quantum-Chemical Study on the Structure, Stability, and Chirality of Protonated Serine Dimers, *Chem. – Eur. J.*, 2005, **11**, 5908–5916.

37 R. R. Julian, R. Hodyss, B. Kinnear, M. F. Jarrold and J. L. Beauchamp, Nanocrystalline Aggregation of Serine Detected by Electrospray Ionization Mass Spectrometry: Origin of the Stable Homochiral Gas-Phase Serine Octamer, *J. Phys. Chem. B*, 2002, **106**, 1219–1228.

38 O. Geller and C. Lifshitz, An electrospray ionization-flow tube study of H/D exchange in the protonated serine dimer and protonated serine dipeptide, *Int. J. Chem. Kinet.*, 2003, **227**, 77–85.

39 F. X. Sunahori, G. Yang, E. N. Kitova, J. S. Klassen and Y. Xu, Chirality recognition of the protonated serine dimer and octamer by infrared multiphoton dissociation spectroscopy, *Phys. Chem. Chem. Phys.*, 2013, **15**, 1873–1886.

40 X. Kong, I. Tsai, S. Sabu, C. Han, Y. T. Lee, H. Chang, S. Tu, A. H. Kung and C. Wu, Progressive Stabilization of Zwitterionic Structures in $[H(Ser)_{2-8}]^+$ Studied by Infrared Photodissociation Spectroscopy, *Angew. Chem., Int. Ed.*, 2006, **45**, 4130–4134.

41 N. Seurre, K. Le Barbu-Debus, F. Lahmani, A. Zehnacker, N. Borho and M. A. Suhm, Chiral recognition between lactic acid derivatives and an aromatic alcohol in a supersonic expansion: electronic and vibrational spectroscopy, *Phys. Chem. Chem. Phys.*, 2006, **8**, 1007–1016.

42 M. E. Crestoni, B. Chiavarino, D. Scuderi, A. Di Marzio and S. Fornarini, Discrimination of 4-hydroxyproline diastereomers by vibrational spectroscopy of the gaseous protonated species, *J. Phys. Chem. B*, 2012, **116**, 8771–8779.

43 A. Sen, K. Le Barbu-Debus, D. Scuderi and A. Zehnacker-Rentien, Mass Spectrometry Study and Infrared Spectroscopy of the Complex Between Camphor and the Two Enantiomers of Protonated Alanine: The Role of Higher-Energy Conformers in the Enantioselectivity of the Dissociation Rate Constants, *Chirality*, 2013, **25**, 436–443.

44 F. Rondino, A. Ciavardini, M. Satta, A. Paladini, C. Fraschetti, A. Filippi, B. Botta, A. Calcaterra, M. Speranza and A. Giardini, *et al.*, Ultraviolet and infrared spectroscopy of neutral and ionic non-covalent diastereomeric complexes in the gas phase, *Rendiconti Lincei*, 2013, **24**, 259–267.

45 R. C. Dunbar, J. D. Steill and J. Oomens, Chirality-Induced Conformational Preferences in Peptide−Metal Ion Binding Revealed by IR Spectroscopy, *J. Am. Chem. Soc.*, 2011, **133**, 1212–1215.

46 A. Bouchet, J. Klyne, S.-I. Ishiuchi, O. Dopfer, M. Fujii and A. Zehnacker, Stereochemistry-dependent structure of hydrogen-bonded protonated dimers: the case of 1-amino-2-indanol, *Phys. Chem. Chem. Phys.*, 2018, **20**, 12430–12443.

47 L. Meng and Z. Lin, Comprehensive computational study of gas-phase conformations of neutral, protonated and deprotonated glutamic acids, *Comput. Theor. Chem.*, 2011, **976**, 42–50.

48 M. Ropo, V. Blum and C. Baldauf, Trends for isolated amino acids and dipeptides: Conformation, divalent ion binding, and remarkable similarity of binding to calcium and lead, *Sci. Rep.*, 2016, **6**, 35772.

49 M. Ropo, M. Schneider, C. Baldauf and V. Blum, First-principles data set of 45 892 isolated and cation-coordinated conformers of 20 proteinogenic amino acids, *Sci. Data*, 2016, **3**, 160009.

50 I. Peña, M. Sanz, J. López and J. Alonso, Preferred Conformers of Proteinogenic Glutamic Acid, *J. Am. Chem. Soc.*, 2011, **134**, 2305–2312.

51 A. Bouchet, J. Klyne, S. Ishiuchi, M. Fujii and O. Dopfer, Conformation of protonated glutamic acid at room and cryogenic temperatures, *Phys. Chem. Chem. Phys.*, 2017, **19**, 10767–10776.

52 J. T. O'Brien, J. S. Prell, J. D. Steill, J. Oomens and E. R. Williams, Interactions of Mono- and Divalent Metal Ions with Aspartic and Glutamic Acid Investigated with IR Photodissociation Spectroscopy and Theory, *J. Phys. Chem. A*, 2008, **112**, 10823–10830.

53 L. Meng and Z. Lin, Complexations of alkali/alkaline earth metal cations with gaseous glutamic acid, *Comput. Theor. Chem.*, 2014, **1039**, 1–10.

54 J. Klyne, A. Bouchet, S.-I. Ishiuchi, M. Fujii and O. Dopfer, Cation-Size-Dependent Conformational Locking of Glutamic Acid by Alkali Ions: Infrared Photodissociation Spectroscopy of Cryogenic Ions, *J. Phys. Chem. B*, 2018, **122**, 2295–2306.

55 S. Ishiuchi, H. Wako, D. Kato and M. Fujii, High-cooling-efficiency cryogenic quadrupole ion trap and UV-UV hole burning spectroscopy of protonated tyrosine, *J. Mol. Spectrosc.*, 2017, **332**, 45–51.

56 R. E. March, An Introduction to Quadrupole Ion Trap Mass Spectrometry, *J. Mass Spectrom.*, 1998, **32**, 351–369.

57 H. Kang, G. Féraud, C. Dedonder-Lardeux and C. Jouvet, New Method for Double-Resonance Spectroscopy in a Cold Quadrupole Ion Trap and Its Application to UV–UV Hole-Burning Spectroscopy of Protonated Adenine Dimer, *J. Phys. Chem. Lett.*, 2014, **5**, 2760–2764.

58 D. J. Wales and J. P. K. Doye, Global Optimization by Basin-Hopping and the Lowest Energy Structures of Lennard-Jones Clusters Containing up to 110 Atoms, *J. Phys. Chem. A*, 1997, **101**, 5111–5116.

59 J. W. Ponder and D. A. Case, Force Fields for Protein Simulations. *Advances in Protein Chemistry: Protein Simulations*, Academic Press, 2003, pp. 27–85.

60 R. V. Pappu, R. K. Hart and J. W. Ponder, Analysis and Application of Potential Energy Smoothing and Search Methods for Global Optimization, *J. Phys. Chem. B*, 1998, **102**, 9725–9742.

61 J.-H. Lii and N. L. Allinger, The MM3 force field for amides, polypeptides and proteins, *J. Comput. Chem.*, 1991, **12**, 186–199.

62 V. Blum, R. Gehrke, F. Hanke, P. Havu, V. Havu, X. Ren, K. Reuter and M. Scheffler, *Ab initio* molecular simulations with numeric atom-centered orbitals, *Comput. Phys. Commun.*, 2009, **180**, 2175–2196.

63 A. Tkatchenko and M. Scheffler, Accurate Molecular van der Waals Interactions from Ground-State Electron Density and Free-Atom Reference Data, *Phys. Rev. Lett.*, 2009, **102**, 73005.

64 Y. Sugita and Y. Okamoto, Replica-exchange molecular dynamics method for protein folding, *Chem. Phys. Lett.*, 1999, **314**, 141–151.

65 M. Rossi and C. Baldauf, Going clean: structure and dynamics of peptides in the gas phase and paths to solvation, *J. Phys.: Condens. Matter*, 2015, **27**, 493002.

66 H. Lei and Y. Duan, Improved sampling methods for molecular simulation, *Curr. Opin. Struct. Biol.*, 2007, **17**, 187–191.

67 X. Daura, K. Gademann, B. Jaun, D. Seebach, W. F. van Gunsteren and A. E. Mark, Peptide Folding: When Simulation Meets Experiment, *Angew. Chem., Int. Ed.*, 1999, **38**, 236–240.

68 H. Berendsen, D. van der Spoel and R. van Drunen, GROMACS: a message-passing parallel molecular dynamics implementation, *Comput. Phys. Commun.*, 1995, **91**, 43–56.
69 A. Tkatchenko, R. A. DiStasio, R. Car and M. Scheffler, Accurate and Efficient Method for Many-Body van der Waals Interactions, *Phys. Rev. Lett.*, 2012, **108**, 236402.
70 S. Chutia, M. Rossi and V. Blum, Water Adsorption at Two Unsolvated Peptides with a Protonated Lysine Residue: From Self-Solvation to Solvation, *J. Phys. Chem. B*, 2012, **116**, 14788–14804.
71 J. Contreras-García, E. R. Johnson, S. Keinan, R. Chaudret, J.-P. Piquemal, D. N. Beratan and W. Yang, NCIPLOT: A Program for Plotting Noncovalent Interaction Regions, *J. Chem. Theory Comput.*, 2011, **7**, 625–632.
72 M. Rossi, M. Scheffler and V. Blum, Impact of Vibrational Entropy on the Stability of Unsolvated Peptide Helices with Increasing Length, *J. Phys. Chem. B*, 2013, **117**, 5574–5584.
73 D. A. Dahl, SIMION for the personal computer in reflection, *Int. J. Mass Spectrom.*, 2000, **200**, 3–25.

